

Tetraquarks from Intrinsic Heavy Quarks

R. Vogt

*Nuclear and Chemical Sciences Division, Lawrence Livermore National Laboratory, Livermore, CA 94551, USA and
Department of Physics and Astronomy, University of California, Davis, CA 95616, USA*

A number of new tetraquark candidate states containing from one to four charm or anti-charm quarks have been observed recently. Many of these new states have been discovered at the LHC. The production of these states via intrinsic charm in the proton is investigated. The tetraquark masses obtained in this approach, while dependent on the internal transverse momenta of the partons in the state, are shown to agree well with the measured masses. These calculations can provide some insight into the nature of the tetraquark candidates, whether as a bound meson pair or as a looser configuration of four individual partons. The kinematic distributions of these states as a function of rapidity and transverse momentum are also studied. The possible cross sections for these states are finally considered, with a comparison to the $X(3872)$ p_T distributions from $p + p$ collisions at $\sqrt{s} = 13$ TeV.

I. INTRODUCTION

Tetraquarks are exotic mesons that are beyond the scope of the conventional quark model of hadrons since they contain four valence quarks. They are denoted as mesons because they include an equal number of quarks and antiquarks. Such states are not ruled out by the Standard Model but have only recently been measured in any quantity. The first tetraquark candidate to be reported, the $X(3872)$, was measured by the Belle Collaboration in 2003 [1]. Later, several other states were discovered by the Belle and BESIII Collaborations, including the $Z(3900)$ [2, 3]. These first confirmed measurements of tetraquark states were made at e^+e^- colliders. Although several other states were reported elsewhere but not all have been confirmed by further analysis [4–7]. Since the advent of the LHC, many new tetraquark candidates have been discovered but still require confirmation in other measurements. A partial list, based on Ref. [8] is given in Table I.

Tetraquarks have long been postulated. Indeed, when Gell-Mann proposed the idea of quarks in 1964, he also suggested that mesons such as $q\bar{q}q\bar{q}$ and baryons such as $qqq\bar{q}$ should exist as well [19]. In 1977 Jaffe discussed properties of $Q^2\bar{Q}^2$ mesons in the context of the bag model [20, 21]. Most models of four particle states like these containing heavy quarks have focused on $q\bar{q}Q\bar{Q}$ states and, indeed, these were the first measured, such the $X(3872)$. The existence of $qq\bar{Q}\bar{Q}$ (and concurrently $\bar{q}\bar{q}QQ$ states) were discussed in Ref. [22]. These types of states were realized by the measurement of the T_{cc}^+ (and its partner the T_{cc}^-) [15]. The body of literature describing the potential structure, spectroscopy, and decays of tetraquarks is large and growing, see reviews in Refs. [23–26, 29] and references therein for more details. Most treat these states as having four constituent quarks but some work also suggests that the $X(3872)$ is an excited $c\bar{c}$ state rather than a tetraquark [27]. (Note also that a nuclear theory topical collaboration, the ExoHad Collaboration [28], was formed to address spectroscopy of exotic hadrons.)

State	Mass (MeV)	Quark Content	Reference
states with 4 charm quarks			
$T_{\psi\psi}(6600)$	6630 ± 90	$c\bar{c}c\bar{c}$	[9]
	6552 ± 16		[10]
$T_{\psi\psi}(6900)$	6905 ± 13	$c\bar{c}c\bar{c}$	[11]
states with 2 charm quarks			
$X(3872)$	3872 ± 0.6	$c\bar{u}c\bar{u}$	[1]
$X_s(3960)$	3955 ± 13	$c\bar{s}c\bar{s}$	[12]
$X_s(4274)$	4273^{+10}_{-9}		[13]
$X_s(4500)$	4506^{+16}_{-19}		[13]
$X_s(4630)$	4630^{+20}_{-110}		[14]
$X_s(4685)$	4684^{+15}_{-17}		[14]
$X_s(4700)$	4704^{+17}_{-26}		[13]
$T_{cc}^+(3876)$	3870 ± 0.12	$cc\bar{u}\bar{d}$	[15]
$T_{c\bar{c}s1}^\theta(4000)$	3991^{+14}_{-20}	$c\bar{c}d\bar{s}$	[16]
$T_{c\bar{c}s1}^+(4220)$	4220^{+50}_{-40}	$c\bar{c}u\bar{s}$	[14]
states with 1 charm quark			
$T_{c\bar{s}0}^a(2900)^0$	2892 ± 21	$c\bar{s}u\bar{d}$	[17]
$T_{c\bar{s}0}^a(2900)^{++}$	2921 ± 25	$c\bar{s}u\bar{d}$	[17]
$T_{cs0}(2900)^0$	2866 ± 7	$c\bar{d}s\bar{u}$	[18]
$T_{cs1}(2900)^0$	2904 ± 5		[18]

TABLE I: Some of the new particles designated as tetraquark candidate states, along with their mass and assigned quark content. Note that the X_s states, as denoted here, are often only referred to as X states. A distinction is made here for the strange quark content. See also Ref. [8].

Table I has been arranged according to the number of charm quarks in the state. A double J/ψ candidate $T_{\psi\psi}(c\bar{c})$ has been observed at two different mass values, 6600 MeV and 6900 MeV. Next are candidates with two light quarks and two charm quarks, followed by candidates with a single charm quark, a $q\bar{q}q\bar{Q}$ configuration. In this latter case, one of the three light quarks is a strange quark.

Most of the tetraquark candidates listed in Table I have quark content $q\bar{q}Q\bar{Q}$ where q or \bar{q} can be u , d , or s quarks.

The heavy quark, Q , can be charm or bottom. So far, all of the candidates reported by the LHC collaborations, see [8], contain charm quarks. No tetraquark candidates with bottom quarks have been measured to date. As previously mentioned, the first $\overline{q}qQQ$ state, the T_{cc}^+ , was observed by LHCb, along with its antiparticle, the T_{cc}^- . The convention quark content given in Table I for the tetraquark candidates is defined with the c quark first. However, this does not mean that the antiparticle is not detected, indeed both the particle and antiparticle are reported together.

This work aims to study the production characteristics of these tetraquark candidates, considering that they are all indeed four-quark states. It assumes that the candidates listed in Table I will be confirmed by other measurements. (So far only the $X(3872)$ is listed in the meson summary tables in the Review of Particle Physics [29].) The calculations are performed within the intrinsic charm model, first developed by Brodsky and collaborators [30, 31] in the early 1980s. In these initial works, only the 5-particle $|uudc\bar{c}\rangle$ configuration of the proton wavefunction was considered for production of c quarks, \overline{D} and J/ψ mesons and the Λ_c baryon.

Later work investigated double J/ψ production measured by the NA3 Collaboration [32, 33] in terms of a 7-particle $|uudc\bar{c}\bar{c}\rangle$ configuration. Good agreement with the NA3 data was found [34]. Recently, a study of double Υ production from a $|uud\bar{b}\bar{b}\bar{b}\rangle$ state showed that the double Υ signal reported by the A_NDY Collaboration [35] was likely not a tetraquark candidate [36]. However, one of the cases considered in Ref. [36] was compatible with the masses of the predicted $\bar{b}\bar{b}b\bar{b}$ tetraquark states [37–42]. (It is worth noting, however that some lattice QCD calculations suggest that $\bar{b}\bar{b}b\bar{b}$ tetraquarks should not be stable [43]. Nonetheless, the compatibility of the calculations in Ref. [36] with the previously-predicted tetraquark masses suggests that the model should be able to predict the charm tetraquark candidate masses with some reasonable accuracy. It may also be possible to learn about the nature of the states, whether they are tightly-bound molecules or loosely-bound four-quark configurations, by studying their mass distributions in this picture.

The intrinsic charm model is introduced and the states required to calculate the tetraquark candidates in Table I are discussed in Sec. II while the calculational structure employed to describe the tetraquark candidate states is discussed in Sec. III. The calculations of the mass (Sec. IV), rapidity and p_T distributions (Sec. V) are described, as well as estimates of the production cross sections (Sec. VI). Conclusions based on the results are given in Sec. VII.

II. INTRINSIC HEAVY FLAVOR PRODUCTION

In QCD, the wave function of a proton can be represented as a superposition of Fock state fluctuations of the basic $|uud\rangle$ state, *e.g.* $|uudg\rangle$, $|uudq\bar{q}\rangle$, $|uudQ\bar{Q}\rangle$. . .

When the proton projectile scatters in a target, either another proton or a nucleus, the coherence of the Fock components is broken by a soft interaction, disrupting the state, so that the fluctuations can hadronize [30, 31, 44]. The model assumes that the soft interaction that disrupts the state is the only a single Fock component of the wavefunction. No interference between Fock state configurations due to simultaneous soft interactions with two states is considered. Such processes may exist, similar to double parton scattering in perturbative QCD but the dominant interaction there, as here, is a single interaction. These Fock state fluctuations are dominated by configurations with equal rapidity constituents. Therefore, the heavy quarks in these states carry a large fraction of the projectile momentum [30, 31]. Thus, even though a soft gluon interaction is all that is required to disrupt the coherence of the state and bring the constituents on shell, the fact that the heavy quark constituents carry a larger momentum fraction means that they can manifest themselves at forward rapidity and large p_T , as discussed in Sec. V.

While the formulation of intrinsic charm by Brodsky and collaborators is used here, other variants of intrinsic charm distributions exist, including meson-cloud models where the proton fluctuates into a $\overline{D}(u\bar{c})\Lambda_c(udc)$ state [45–48], also resulting in forward production, or a sea-like distribution [49, 50], only enhancing the distributions produced by massless parton splitting functions as in DGLAP evolution. Intrinsic charm has also been included in global analyses of the parton densities [49–56]. (See Ref. [57] for a discussion of a possible kinematic constraint on intrinsic charm in deep-inelastic scattering.)

The probability of intrinsic charm production from a 5-particle state, P_{ic5}^0 , obtained from these analyses, as well as others, has been suggested to be between 0.1% and 1%, see the reviews in Refs. [58, 59] for discussions of the global analyses and other applications of intrinsic heavy quark states. Evidence of a finite charm quark asymmetry in the nucleon wavefunction from lattice gauge theory, consistent with intrinsic charm, was presented in Ref. [60].

Heavy quark hadrons can be formed from these intrinsic heavy quark states by coalescence of the partons in the states with each other to form either pairs of charm hadrons, such as a $\Lambda_c^+(udc)$ and $D^0(u\bar{c})$ or a $\Sigma_c^{++}(uuc)$ and $D^-(d\bar{c})$, or a J/ψ and a proton from a $|uudc\bar{c}\rangle$ state. The final-state hadron is identified by its quark content and is assumed to come on shell with its correct quantum numbers (J^{PC}) via a nonperturbative process, similar to hadron production in perturbative QCD.

The D^0 or D^- mesons so produced have referred to as leading charm because they can be produced from the smallest possible Fock state configuration with a $c\bar{c}$ pair. Non-leading charm, D^+ and \overline{D}^0 , production by intrinsic charm requires at least a 7-particle Fock state of the proton with an additional light quark-antiquark pair, $|uudc\bar{c}q\bar{q}\rangle$. Note that in this case, however, $D\overline{D}$ pairs are produced, D^+D^- or $D^0\overline{D}^0$. Thus these D mesons would

be produced with the same momentum distributions from this state and neither is leading. Asymmetries between leading and nonleading charm have been measured as a function of p_T and Feynman x , x_F , or rapidity in fixed-target $\pi^- + p$ interactions [61–63] and in fixed-target $p + A$ interactions measured with the SMOG device at LHCb [64]. Both scenarios have been calculated within the intrinsic charm picture [65, 66]. Good agreement with the $\pi^- + p$ data was found in Ref. [65] while the asymmetry at low p_T and near central rapidity in $p + \text{Ne}$ interactions was underestimated in Ref. [66].

In this work, the tetraquark candidate states are assumed to be produced from the minimum possible Fock state required for their production. In most cases, this is a 7-particle state. For the remainder, 9-particle states are required. Although Fock states with greater quark content could be considered, these should be less dominant, as described below. First, higher Fock states will have lower probabilities for production, *i.e.* $P_{ic5}^0 > P_{ic7}$. Still higher Fock states will have correspondingly lower probabilities. Since the relative production probability is proportional to the square of the quark masses [36], adding light quark-antiquark pairs to the state results in a smaller mass penalty than adding a heavy $Q\bar{Q}$ pair, as discussed in Sec. VI. Second, as already mentioned, adding light $q\bar{q}$ pairs to the state results in no distinction between leading and nonleading D meson production from this state and, in fact, reduces the asymmetry when such contributions are included [67]. In addition, D mesons from higher Fock states would have lower average rapidity or x_F relative to the minimal Fock state.

Because only 7- and 9-particle Fock states are employed in these calculations, in some cases, only the antiparticle of the candidate given in Table I will be con-

sidered. For example, production of $T_{cc}^+(cc\bar{u}\bar{d})$ would require an 11-particle Fock state, $|uud\bar{c}\bar{c}cc\bar{u}\bar{u}\bar{d}\bar{d}\rangle$, for production. However, its antiparticle partner $T_{cc}^-(\bar{c}\bar{c}ud)$ requires only a 7-particle Fock state, $|uud\bar{c}\bar{c}\bar{c}\bar{c}\rangle$, for production. An 11-particle Fock state, $|uud\bar{c}\bar{c}\bar{s}\bar{s}\bar{u}\bar{u}\bar{d}\bar{d}\rangle$, is required for $T_{cs}(2900)^0(c\bar{d}\bar{s}\bar{u})$ production while its antiparticle $T_{cs}^0(\bar{c}\bar{d}\bar{s}u)$ can be produced from a 7-particle state, $|uud\bar{c}\bar{c}\bar{s}\bar{s}\rangle$. Thus, in these cases, the tetraquark candidates and their antiparticles will not have identical kinematic distributions according to the model and the antiparticles will be ‘leading’. On the other hand, the $T_{\bar{c}s1}(\bar{c}\bar{c}q\bar{s})$ can be produced from a 7-particle $|uud\bar{c}\bar{c}\bar{s}\bar{s}\rangle$ state and is thus leading while production of the antiparticle requires a 9-particle state, $|uud\bar{c}\bar{c}\bar{s}\bar{s}q\bar{q}\rangle$, for production.

In previous work, the cross sections of J/ψ and D mesons from intrinsic charm have been calculated and compared with perturbative production cross sections [66, 68]. Though similar calculations of the cross sections for tetraquark production from intrinsic charm states can be made, including the appropriate additional suppression factors for production from higher Fock states, here unit normalized distributions are shown in this proof-of-principle calculation. See Sec. VI for estimates of the upper limits of the cross sections.

III. CALCULATIONAL STRUCTURE

The frame-independent probability distribution of a n -particle Fock state in the proton containing at least one $c\bar{c}$ pair is [30, 31]

$$dP_{icn} = P_{icn}^0 N_n \int dx_1 \cdots dx_n \int dk_{x1} \cdots dk_{xn} \int dk_{y1} \cdots dk_{yn} \frac{\delta(1 - \sum_{i=1}^n x_i) \delta(\sum_{i=1}^n k_{xi}) \delta(\sum_{i=1}^n k_{yi})}{(m_p^2 - \sum_{i=1}^n (m_{T_i}^2/x_i))^2}, \quad (1)$$

where $n = 7$ and 9 are the highest Fock states considered for tetraquarks containing at least a single charm quark, as in Table I. Here N_n normalizes the probability to unity and P_{icn}^0 scales the unit-normalized probability to the assumed intrinsic charm content of the proton. The delta functions conserve longitudinal (z) and transverse (x and y) momentum. The denominator of Eq. (1) is minimized when the heaviest constituents carry the largest fraction of the longitudinal momentum, $\langle x_c \rangle > \langle x_q \rangle, \langle x_s \rangle$.

In Table II, the tetraquark states from Table I are shown, along with the minimal Fock state required to produce them. The indices 1-9 on the top row correspond to the particle assignments in the calculations of the probability distributions according to Eq. (1). To ease the calculation, the tetraquark candidates are as-

signed to $i = 4 - 7$ in an n -particle state. If one imagines the tetraquark candidate as a meson pair, one of the mesons is assigned to be the combination of indices 4 + 7 while the other is assigned indices 5 + 6. The numerical calculations in this work based on Eq. (1) are carried out using the VEGAS code [69], allowing up to 25 dimensional integration.

Note that the model makes no distinction between u and d quarks, both are assumed to have the same mass. Therefore, the $T_{\bar{c}s1}^0(c\bar{c}\bar{d}\bar{s})$ and the $T_{\bar{c}s1}^+(\bar{c}\bar{c}u\bar{s})$ will be calculated and referred to as $T_{\bar{c}s1}$ in the remainder of this work. Similarly, the $T_{csp}^0(c\bar{s}u\bar{d})$ and $T_{csp}^{a++}(c\bar{s}u\bar{d})$ will be referred to as T_{cs0}^a . In addition, the T_{cs1}^0 and T_{cs0}^0 from Table I, with the same assumed quark content ($\bar{c}\bar{d}\bar{s}u$), are listed in Table II simply as T_{cs}^0 .

State	Quark content	Fock state	1	2	3	4	5	6	7	8	9
$T_{\psi\psi}$	$c\bar{c}c\bar{c}$	$ uudc\bar{c}c\bar{c}\rangle$	u	u	d	c	\bar{c}	c	\bar{c}	-	-
$X(3872)$	$c\bar{u}c\bar{u}$	$ uudc\bar{c}c\bar{c}\rangle$	u	u	d	c	\bar{c}	u	\bar{u}	-	-
X_s	$c\bar{s}c\bar{s}$	$ uudc\bar{c}s\bar{s}\rangle$	u	u	d	c	\bar{c}	s	\bar{s}	-	-
T_{cc}^-	$\bar{c}c\bar{u}d$	$ uudc\bar{c}c\bar{c}\rangle$	u	c	c	\bar{c}	u	\bar{c}	d	-	-
$T_{c\bar{c}s}^0$	$\bar{c}c\bar{d}s$	$ uudc\bar{c}s\bar{s}\rangle$	u	u	s	c	\bar{s}	d	\bar{c}	-	-
$T_{c\bar{c}s}^+$	$\bar{c}c\bar{u}s$	$ uudc\bar{c}s\bar{s}\rangle$	u	d	s	c	\bar{s}	u	\bar{c}	-	-
T_{cs}^0	$\bar{c}d\bar{s}u$	$ uudc\bar{c}s\bar{s}\rangle$	u	c	s	\bar{c}	\bar{s}	u	d	-	-
T_{cs0}^{a0}	$\bar{c}s\bar{u}d$	$ uudc\bar{c}s\bar{s}u\bar{u}\rangle$	u	u	u	c	\bar{u}	d	\bar{s}	\bar{c}	s
T_{cs0}^{a++}	$\bar{c}s\bar{u}d$	$ uudc\bar{c}s\bar{s}d\bar{d}\rangle$	u	d	d	c	\bar{d}	u	\bar{s}	\bar{c}	s

TABLE II: The quark content of each type of tetraquark candidate considered in this work is given. The population of the minimal Fock state required to product the tetraquark candidate is also given, along with the parton assignments used to calculate the mass distributions in Eqs. (2) and (3). Note that the T_{cs1}^0 and T_{cs0}^0 from Table I, with the same assumed quark content, are listed simply as T_{cs}^0 .

In Ref. [70], the J/ψ p_T distribution from intrinsic charm was calculated for the first time by integrating over the light and charm quark k_T ranges in Eq. (1). In that work, k_{Tq}^{\max} was set to 0.2 GeV while the default for k_{Tc}^{\max} was taken to be 1 GeV. The sensitivity of the results to the k_T integration range was tested by multiplying the maximum of the respective k_T ranges by 0.5 and 2 respectively. As shown in Fig. 4 of Ref. [70], the average p_T of a J/ψ is slightly reduced for the smaller k_{Tc}^{\max} but it only narrows the p_T distribution slightly, giving a final J/ψ p_T distribution closer to that of a single charm quark. On the other hand, doubling the range of k_{Tc}^{\max} leads to a significantly wider p_T distribution. One could consider the k_T range as a proxy for coherence of the bound state when calculating the mass distributions of the tetraquark states, as discussed in Sec. IV.

The k_T range can be considered to represent the extent of the internal motion of the partons in the final-state hadron, with a low k_T range corresponding to a more tightly bound state, with a lower mass and a narrower width. A higher k_T range would allow for more internal motion of the partons, giving a wider width and a correspondingly larger size. Thus different sets of k_T integration ranges can be associated with excited states of the same meson, such as the difference between the $T_{psipsi}(6600)$ and (6900), similar to the difference in mass and radius between the J/ψ and the $\psi(2S)$ in charmonium spectroscopy.

Several different scenarios are considered for the transverse momentum ranges of the quarks and constituent mesons of the tetraquark states. They are given in Table III. The set kt1 takes the default values used for J/ψ and \bar{D} meson calculations in Refs. [66, 68] while with sets kt2 and kt3 the range is halved (for a more tightly bound state) and doubled (for a more weakly bound state). A fourth set, kt4, takes values 50% higher than those of

Set	k_q^{\max} (GeV)	k_s^{\max} (GeV)	k_c^{\max} (GeV)	k_{TQ}^{\max} (GeV)
kt1	0.2	0.4	1.0	1.0
kt2	0.1	0.2	0.5	0.5
kt3	0.4	0.8	2.0	2.0
kt4	0.3	0.6	1.5	1.5

TABLE III: The four sets of maximum range of k_T integration for light quarks, strange quarks (when applicable), charm quarks, and the tetraquark state in the proton, designated by the subscript TQ here.

kt1.

The quark masses used in the calculation of the transverse masses in Eq. (1) are $m_q = 0.01$ GeV, $m_s = 0.3$ GeV and $m_c = 1.27$ GeV, effectively current quark masses. The kinematic distribution can be calculated assuming simple coalescence of the quark in the state described in Eq. (1) by adding the appropriate delta functions in the x and k_T directions.

As shown in Ref. [68], while the x_F distribution is independent of k_T and initial energy, the rapidity distribution is boosted in the direction of the incident proton. One starts with the calculation of the x_F distribution and uses a Jacobean in the integral to transform to rapidity. The x_F or rapidity-integrated p_T distribution does not depend on the center of mass energy of a collision bringing a tetraquark state in the proton, as in Eq. (1), on mass shell. However, the p_T distribution in a specific rapidity region is significantly modified. The higher the energy, the more the average p_T is moved to higher p_T at midrapidity. The distribution is suppressed less at forward rapidity in high energy collisions, see Ref. [68]. This will be discussed in more detail in Sec. V.

IV. TETRAQUARK MASS DISTRIBUTIONS

In these calculations, charm tetraquark production is first assumed to occur only as a pair of charm mesons for states with two or more charm quarks. In these cases, the masses of the two meson components are well balanced and a mass peak can be found. This is the case for $T_{\psi\psi}$, $X(3872)$, X_s and T_{cc}^- . If one considers the $T_{c\bar{c}s}$ as a $(c\bar{c}) + (q\bar{s})$ meson pair or the T_{cs} states as either $D_s(c\bar{s}) + \pi(q\bar{q}')$ for $T_{c\bar{c}s}$ or $D^+(c\bar{d}) + K^-(s\bar{u})$ for T_{cs} , one does not find a distribution with a clear maximum mass because the light meson could be described as orbiting the heavy charm meson with higher masses corresponding to larger distances between the two. However, if these states are simply described as an uncorrelated cluster of two quarks and two antiquarks, the state is stable with a finite mass.

Such differences in the stability of the state based on the assumed internal structure can result in different final-state properties that could be distinguished in other production processes. For example, in heavy-ion collisions, tetraquark candidates that can exist as a pair

of bound mesons may be harder to break up in the produced hot medium than those that are made up of four independent partons. On the other hand, one might expect that tetraquarks could also be produced by recombination of constituent partons within sufficiently close proximity in high multiplicity heavy-ion collisions, as discussed in Refs. [71, 72].

In this section, the two ways of calculating the tetraquark mass distributions are described. The calculated mass distributions from both cases are shown in

Sec. IV C.

A. Tetraquark Production as a Meson Pair

If the tetraquark is considered to be a bound pair of mesons, the mass distribution can be calculated as [34, 36]

$$\begin{aligned}
 \frac{dP_{icn}}{dM_{TQ}^2} &= \int \frac{dx_{M_1}}{x_{M_1}} \frac{dx_{M_2}}{x_{M_2}} \int dm_{M_1}^2 dm_{M_2}^2 \int dk_{xM_1} dk_{yM_1} dk_{xM_2} dk_{yM_2} \int \frac{dx_{TQ}}{x_{TQ}} \int dk_{xTQ} dk_{yTQ} dP_{icn} \\
 &\times \delta\left(\frac{m_{T,M_1}^2}{x_{M_1}} - \frac{m_{T4}^2}{x_4} - \frac{m_{T7}^2}{x_7}\right) \delta(k_{x4} + k_{x7} - k_{xM_1}) \delta(k_{y4} + k_{y7} - k_{yM_1}) \delta(x_{M_1} - x_4 - x_7) \\
 &\times \delta\left(\frac{m_{T,M_2}^2}{x_{M_2}} - \frac{m_{T5}^2}{x_5} - \frac{m_{T6}^2}{x_6}\right) \delta(k_{x5} + k_{x6} - k_{xM_2}) \delta(k_{y5} + k_{y6} - k_{yM_2}) \delta(x_{M_2} - x_5 - x_6) \\
 &\times \delta\left(\frac{M_{T,TQ}^2}{x_{TQ}} - \frac{m_{T,M_1}^2}{x_{M_1}} - \frac{m_{T,M_2}^2}{x_{M_2}}\right) \delta(k_{xM_1} + k_{xM_2} - k_{xTQ}) \delta(k_{yM_1} + k_{yM_2} - k_{yTQ}) \delta(x_{TQ} - x_{M_1} - x_{M_2}) \quad (2)
 \end{aligned}$$

where dP_{icn} is taken from Eq. (1). As written here, the pair mass distributions require integration over the invariant mass of each meson of the pair, M_1 and M_2 , over some suitable range. In the calculation of $T_{\psi\psi}$ in this work, as well as previous calculations of double J/ψ [34] and Υ [36] production, the range is between twice the heavy quark mass and twice the mass of the lowest mass heavy meson, $2m_Q < m_{TM} < 2m_H$. In the other cases, where charm mesons are considered, a delta function, $\delta(m_{M_i}^2 - m_{M_{\text{meson}}}^2)$ is employed to integrate over $dm_{M_i}^2$. For example, to calculate $X(3872)$, m_{M_1} and m_{M_2} are taken to be m_{D^0} and $m_{\bar{D}^0}$ respectively. The delta functions ensure conservation of momentum for both mesons in the pair as well as the tetraquark candidate. The tetraquark candidate is labeled by the subscript TQ.

The mass-dependent delta functions in Eq. (2) can be considered to constitute the minimal assumption of a tetraquark wavefunction in the intrinsic heavy quark state. In this case, the delta functions for mesons M_1 and M_2 represent a two-body wavefunction for each meson while that for M_{TQ} represents the two-body meson-pair wavefunction. Thus the constituents of each two-body system can have any kinematics that does not exceed the k_T cutoffs as long as each system conserves momentum. The k_T ranges emphasized in Table III are thus related to how tightly the mesons and the tetraquark itself are bound.

As was shown in Ref. [36], the k_T integration range affects the mass distributions. A narrower k_T integration range resulted in a mass distribution with a lower average

value and a narrower width. Thus specific k_T ranges can differentiate between excited states. This possibility is explored for the $X_s(c\bar{c}s)$ states in this section.

Note that current quark masses are used in these calculations because m_M has to be larger than $\hat{m}_{T,i}$ for the delta functions describing the mass differences in Eq. (2) to have a solution. This condition would not be satisfied if constituent quark masses are employed for *e.g.* $T_{c\bar{c}s1}$ as a $(c\bar{c})(q\bar{s}) \equiv J/\psi + K$ meson pair because $m_q + m_s > m_K$ if constituent quark masses are used. Even employing these masses, the probability as a function of tetraquark candidate mass rises with M_{TQ} rather than exhibiting a resonance structure. This is because, unlike a bound meson pair of two nearly equal objects orbiting around each other, the physical picture is more like a light object orbiting around a stationary heavy object. Higher values of M_{TQ} imply a larger radius where the lighter meson orbits further away from the heavy one. Therefore, these systems are treated as a cluster of four independent quarks, as shown in the next section.

B. Tetraquark Production as a Four Quark State

Here the constraint that the four quarks in a tetraquark candidate are considered to be part of a meson-antimeson pair is relaxed. If the four quarks constituting a tetraquark candidate are considered as a single cluster, the mass distribution for M_{TQ} is then [36]

$$\frac{dP_{icn}}{dM_{TQ}^2} = \int \frac{dx_{TQ}}{x_{TQ}} \int dk_{xTQ} dk_{yTQ} dP_{icn} \delta \left(\frac{M_{T,TQ}^2}{x_{TQ}} - \frac{m_{T,4}^2}{x_4} - \frac{m_{T,5}^2}{x_5} - \frac{m_{T,6}^2}{x_6} - \frac{m_{T,7}^2}{x_7} \right) \times \delta(k_{x4} + k_{x5} + k_{x6} + k_{x7} - k_{xTQ}) \delta(k_{y4} + k_{y5} + k_{y6} + k_{y7} - k_{yTQ}) \delta(x_{TQ} - x_4 - x_5 - x_6 - x_7), \quad (3)$$

where dP_{icn} is from Eq. (1). Under this assumption, the $T_{c\bar{c}s1}$, $T_{c\bar{c}0}^a$, and T_{cs}^0 mass distributions all have a discernible mass peak.

In this case the mass-dependent delta functions in Eq. (2) are replaced by a single delta function connecting the four quarks in the states independently rather than considering them as constituents of mesons internal to the tetraquark wavefunction. Here the k_T ranges in Table III set the scale for the proximity of the individual quarks in momentum space rather than as partners in a meson.

The mass distributions for both assumptions of the tetraquark structure, Eqs. (2) and (3), are shown in the next section.

C. Calculated Mass Distributions

This section presents the mass distributions calculated as described in the previous subsections. The average masses and widths will also be reported. The average masses, calculated using both Eqs. (2) and (3), as discussed in the preceding sections, can be found in Table IV. The widths of the distributions are given in Table V. The widths are calculated as the standard deviation of the mass distributions. Thus, if the mass is defined as the average over the distribution, $\langle M_{TQ} \rangle$, the variance of the distribution is $\langle M_{TQ}^2 \rangle - \langle M_{TQ} \rangle^2$ and the standard deviation is the square root of the variance.

Because the focus here is on production by coalescence, with no constraints other than the momentum-conserving delta functions, the model cannot reproduce the masses and widths of the tetraquark candidates on the few-MeV or lower scales of the measured values, but only on the order of several hundred MeV. As will be shown, the masses are in rather good agreement with the measured values without introducing further constraints. The widths are, unsurprisingly, considerably overestimated.

The first set of mass distributions, corresponding to states that can be calculated under the assumption that the state is produced as a meson pair, are shown in Sec. IV C 1. The second set of distributions, assuming the tetraquark is produced as a four-quark state, are shown in Sec. IV C 2. All mass distributions shown have the probability normalized to unity since the focus is on the shape of the distributions. The possible production cross sections are discussed in Sec. VI.

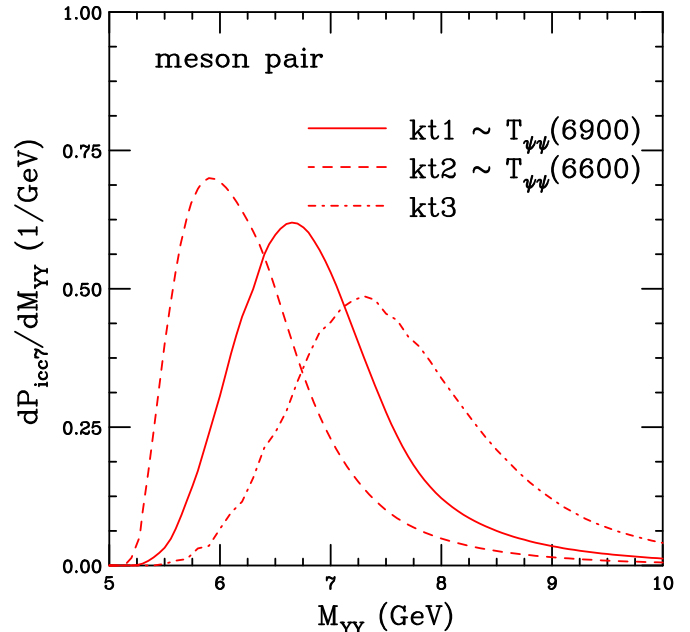


FIG. 1: The $T_{\psi\psi}$ probability distribution, calculated using Eq. (2), as a function of mass of the state. Calculations are shown for kt1 (solid), kt2 (dashed), and kt3 (dot-dashed).

1. Meson Pair Distributions

The mass distributions of the $T_{\psi\psi}$, with four charm quarks, $c\bar{c}c\bar{c}$, are shown first. Then the $X(3872)$, the X_s states, and the T_{cc}^- , all calculated assuming the state consists of a $D\bar{D}$ or $D_s\bar{D}_s$ meson pair, are shown.

Figure 1 shows the results for the $T_{\psi\psi}$ for three of the four k_T ranges: kt1, kt2 and kt3. The distributions are all rather broad, with the distributions becoming broader as the k_T integration range is increased. There is a distinct shift to higher average masses with increasing maximum k_T . The lowest k_T maximum, corresponding to kt2, gives the lowest average mass, approximately consistent with the $T_{\psi\psi}(6600)$, $M = 6.36$ GeV. The k_T maximum used as the default in Ref. [36], kt1, gives an average mass consistent with $T_{\psi\psi}(6900)$, 6.93 GeV. The average mass of all three cases can be found in Table IV. The widths of the distributions are given in Table V. They are between 0.75 and 0.9 GeV with the narrowest width associated with the lowest mass.

The mass distributions for the $X(3872)$ are shown in Fig. 2. The average mass assuming set kt1 for the k_T

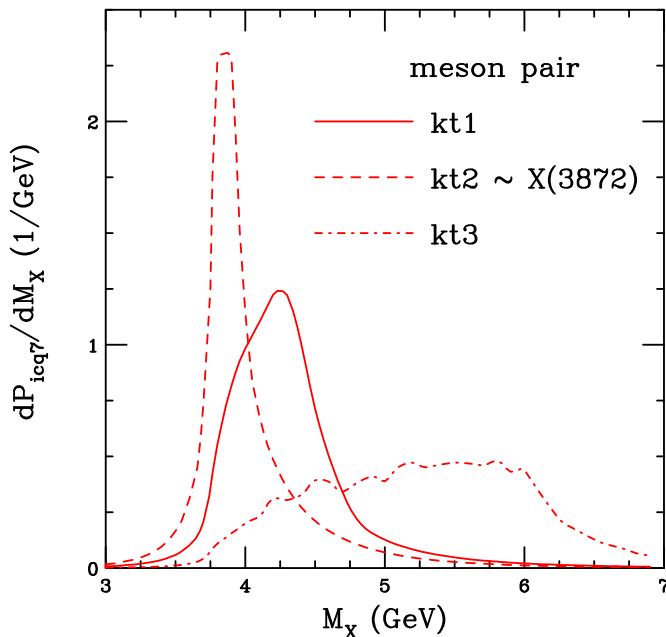


FIG. 2: The $X(3872)$ probability distribution, calculated using Eq. (2), as a function of mass of the state. Calculations are shown for kt1 (solid), kt2 (dashed), and kt3 (dot-dashed).

range is 4.3 GeV, significantly larger than the mass of the X but could be in agreement with an excited state of the X , as seen for $T_{\psi\psi}$ in Fig. 1. However, when the narrower range of set kt2 is used, the average mass is 4.0 GeV, only approximately 0.1 GeV more than the measured mass. In addition, the width in this case is 0.42 GeV, broader than the measured width but resulting in a rather narrow peak nonetheless. Doubling the k_T range, with set kt3, results in a broader distribution with a width of ~ 0.74 GeV.

Given the rather good agreement of set kt2 with the measured $X(3872)$ mass, most of the calculations of the kinematic distributions in Sec. V will employ this assumption. Exceptions will be made for the $T_{\psi\psi}$ and the X_s states which have reported more than one mass state.

Figure 3 shows the mass distributions of the states labeled X_s here, with $c\bar{s}\bar{c}s$ content, effectively a tetraquark state composed of a $D_s\bar{D}_s$ pair. Based on Table I, the measured X_s states can be approximately grouped into masses of 4.0, 4.55 and 4.7 GeV. To better approximate these masses, set kt4 was introduced with a k_T range intermediate between sets kt1 and kt3. Indeed, the calculations shown in Fig. 3 for sets kt2, kt1 and kt4, with average masses of 4.2, 4.5 and 4.9 GeV respectively, are in rather good agreement with these approximate masses. More fine tuning of the k_T range could separate individual masses further.

The width increases slowly with the k_T range. The widths with sets kt1 and kt2 are similar, 0.43 GeV, while the width with set kt4 is 0.53 GeV. The average mass and corresponding width employing set kt2 is somewhat

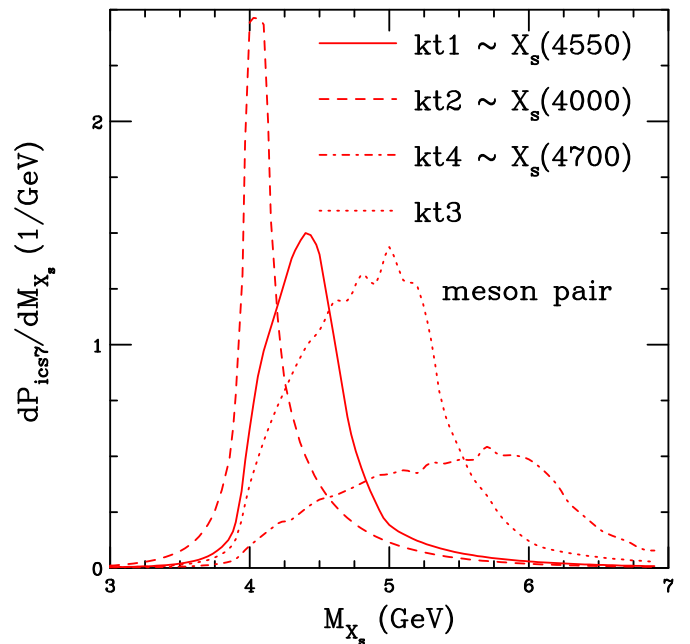


FIG. 3: The X_s probability distributions, calculated using Eq. (2), as a function of mass of the state. Calculations are shown for kt1 (solid), kt2 (dashed), kt3 (dot-dashed) and kt4 (dotted). The approximately grouped X_s masses based on Table I are associated with the closest k_T range.

higher than that for the $X(3872)$ in Fig. 2 because the light $q\bar{q}$ in the 7-particle Fock state for the $X(3872)$ is replaced by the heavier $s\bar{s}$ pair.

Figure 4 compares the mass distributions of the $X(3872)$, X_s and T_{cc}^- for set kt2. The mass shift between the $X(3872)$ and the X_s with $M \approx 4.0$ GeV is apparent, as is the somewhat broader width. The T_{cc}^- mass is almost identical to that of the $X(3872)$, as may be expected due to the nearly identical quark content. Its width is also similar, 0.5 MeV compared to 0.4 MeV for the $X(3872)$.

2. Mass Distributions Assuming a Four-Quark State

Here the mass distributions of tetraquark states assumed to be composed of loosely bound 4-quark states are shown. These states have either one charm quark or, in the case of $T_{c\bar{c}s}$, the c and \bar{c} quarks are assumed to form a “ ψ ” rather than connect to the light quarks in the state. If the c and \bar{c} are assumed to be associated with each other as in a J/ψ , no well-defined mass can be obtained. However, if one, on the other hand, assumed that the parton configuration was $(c\bar{q})(c\bar{s}) \equiv DD_s$, one could calculate this state in a meson pair configuration. The masses given in Table I are similar to the two lowest masses given for the X_s tetraquark candidates.

The $T_{c\bar{c}s}$ mass distributions are shown in Fig. 5. As

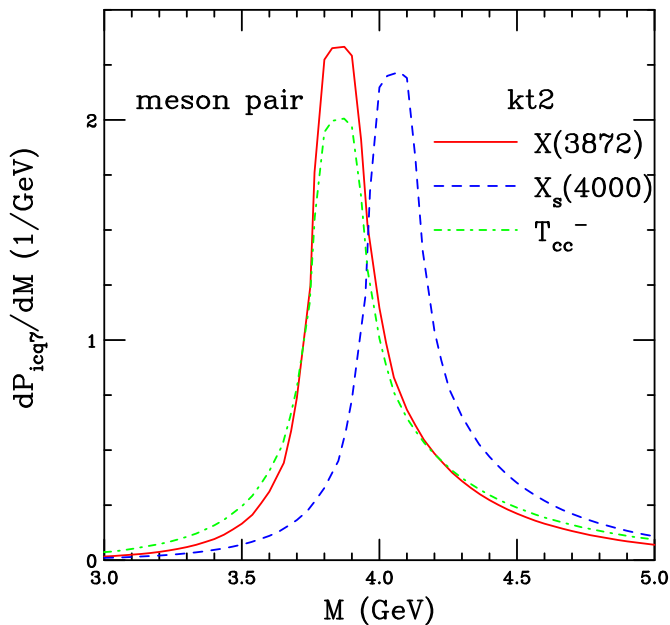


FIG. 4: The probability distributions for $X(3872)$ (red solid), X_s (blue dashed) and T_{cc}^- (dot-dashed green), calculated using Eq. (2), as a function of mass of the state for scenario kt2.

in the previous section, the distributions with larger k_T ranges have larger average masses. However, now since the quarks are not assumed to pair into mesons but exist in a more loosely bound configuration, the widths are considerably larger, even for the narrowest distribution calculated with set kt2. The average mass with this set, 4.3 GeV, is very similar to that of the X_s calculated with set kt2 but the width is now ~ 0.8 GeV instead of the value of 0.4 GeV obtained for the X_s calculated with the same k_T set.

Figures 6 and 7 compare the mass distributions calculated from a 7-particle state for $T_{cs0}(2900)^0$ and $T_{cs1}(2900)^0$ (both labeled T_{cs}^0 in the figure) and from a 9-particle state for $T_{cs0}^a(2900)^0$ and $T_{cs0}^a(2900)^{++}$ (both labeled T_{cs0}^a in the figure). Recall that in the former case, the antiparticle partner, $\bar{c}d\bar{s}u$, is calculated since producing a $c\bar{d}s\bar{u}$ state in the intrinsic charm model requires a sub-leading 11-particle state.

Despite the additional light $q\bar{q}$ pair required to produce the T_{cs0}^a , the mass distributions in Fig. 7 are remarkably similar to those of the T_{cs}^0 in Fig. 6, giving nearly equal masses and very similar widths. In fact, this should not be particularly surprising because employing the same quark flavors in the tetraquark state should yield a similar mass distribution, regardless of how many quarks are in the initial proton wavefunction. Only the kinematic distributions depend on the number of particles in the initial proton Fock configuration, as will be shown in Sec. V.

In both cases, the average mass with set kt2 is ≈ 3.3 GeV, comparable to but slightly larger than the mea-

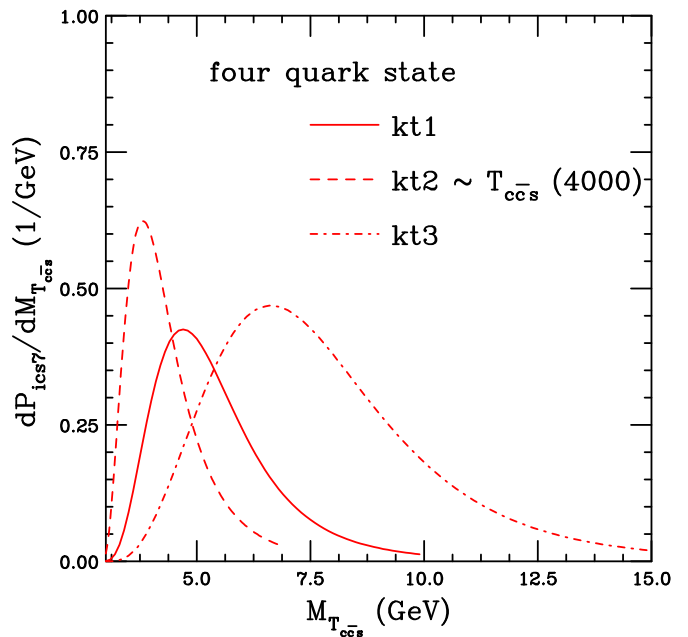


FIG. 5: The T_{ccs}^- probability distribution, calculated using Eq. (3), as a function of mass of the state. Calculations are shown for kt1 (solid), kt2 (dashed), and kt3 (dot-dashed).

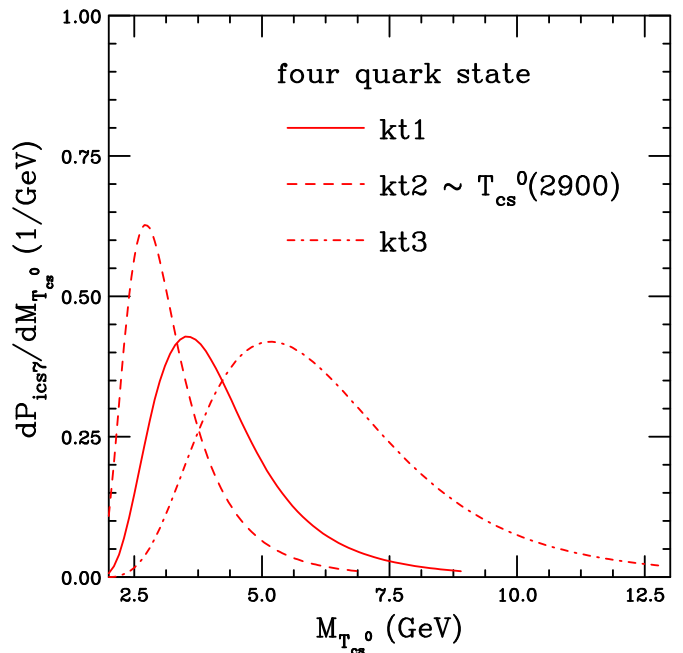


FIG. 6: The T_{cs}^0 probability distribution, calculated using Eq. (3), as a function of mass of the state. Calculations are shown for kt1 (solid), kt2 (dashed), and kt3 (dot-dashed).

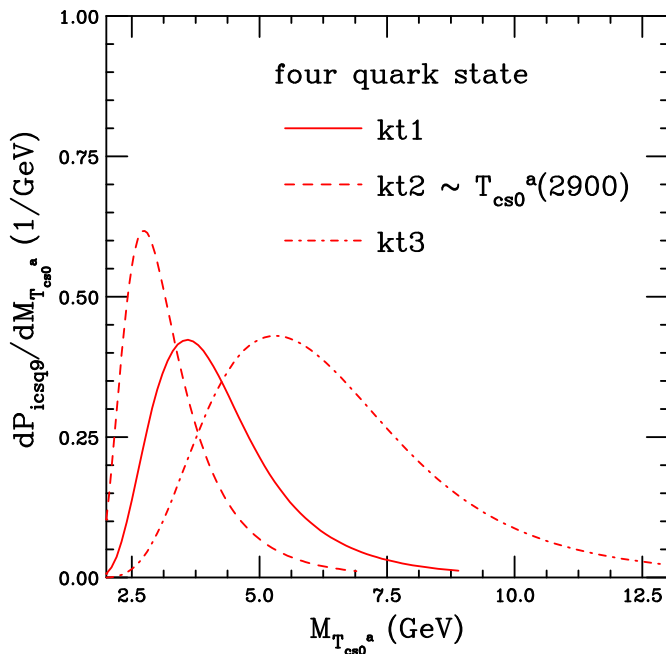


FIG. 7: The T_{cs0}^a probability distribution, calculated using Eq. (3), as a function of mass of the state. Calculations are shown for kt1 (solid), kt2 (dashed), and kt3 (dot-dashed).

sured mass of the state. The widths, with set kt2, are ≈ 0.9 GeV, slightly larger than the width calculated for the $T_{c\bar{c}s}$.

State	Mass (GeV)			
	kt1	kt2	kt3	kt4
Meson pair configuration				
$T_{\psi\psi}$	6.933	6.358	7.637	-
$X(3872)$	4.303	4.021	5.236	-
X_s	4.475	4.215	5.404	4.892
$T_{c\bar{c}}^-$	4.349	4.054	5.394	-
4-quark configuration				
$T_{c\bar{c}s}$	5.404	4.301	7.716	-
T_{cs}^0	4.218	3.263	6.261	-
T_{cs0}^a	4.272	3.288	6.394	-

TABLE IV: The average tetraquark candidate mass from intrinsic charm states for the k_T integration range given. Note that only the X_s calculation uses set kt4. Note also that T_{cs}^0 refers to both T_{cs1}^0 and T_{cs0}^0 while T_{cs0}^a refers to both $T_{c\bar{s}0}^a$ and T_{cs0}^{a++} .

Overall, the agreement between the calculations and the measured tetraquark candidate masses is quite good. The calculations can also distinguish between assumptions about the nature of the tetraquarks, as either a pair of D or D_s mesons or as a more loosely bound 4-quark

State	Width (GeV)			
	kt1	kt2	kt3	kt4
Meson pair configuration				
$T_{\psi\psi}$	0.797	0.748	0.905	-
$X(3872)$	0.456	0.422	0.739	-
X_s	0.431	0.432	0.702	0.534
$T_{c\bar{c}}^-$	0.515	0.510	0.732	-
4-quark configuration				
$T_{c\bar{c}s}$	1.264	0.783	2.212	-
T_{cs}^0	1.251	0.883	2.057	-
T_{cs0}^a	1.270	0.895	2.087	-

TABLE V: The width (standard deviation) of the tetraquark candidate mass distribution from intrinsic charm states for the k_T integration range given. Note that only the X_s calculation uses set kt4. Note also that T_{cs}^0 refers to both T_{cs1}^0 and T_{cs0}^0 while T_{cs0}^a refers to both $T_{c\bar{s}0}^a$ and T_{cs0}^{a++} .

state. For example, a tetraquark with the composition $c\bar{c}d\bar{s}$ could be arranged either as $(c\bar{s}) + (\bar{c}d) \equiv D_s^+ + D^-$ or $(c\bar{c}) + (d\bar{s}) \equiv J/\psi + K^0$. In the former case, where the lighter d or \bar{s} quark is associated with a heavy charm quark, the meson pair assumption can be used. In the latter, case, as discussed earlier in this section, one can obtain a defined mass peak only if the state is assumed to be composed of four uncorrelated quarks.

V. TETRAQUARK KINEMATIC DISTRIBUTIONS

The rapidity and p_T distributions of the states discussed in the previous section are now calculated. In this section, for ease of calculation, instead of integrating over the tetraquark mass, the average masses are used instead. As in the previous section, all distributions are shown normalized to unity to facilitate comparison of the shapes of the distributions.

The denominator of Eq. (1) ensures that the heaviest quarks in the state carry the largest fraction of the momentum. This can be manifested by the charm quarks either carrying a larger fraction of the longitudinal momentum, represented by Feynman x , or x_F , or larger transverse momentum. The number of quark in the state also plays a role in their kinematic distributions: when the available momentum is distributed among more partons, the average phase space available to each one is reduced.

To demonstrate how the number of quarks in the state might affect the kinematic distributions, in Figs. 8 and 9, the charm quark Feynman x and p_T distributions are shown for 5-, 7- and 9-particle states of the proton. To standardize the result, only light $q\bar{q}$ pairs are added to the $|uudc\bar{c}\rangle$ state, *i.e.* $|uudc\bar{c}q\bar{q}\rangle$ and $|uudc\bar{c}q\bar{q}q\bar{q}\rangle$. Note that q can represent u or d quarks interchangeably because

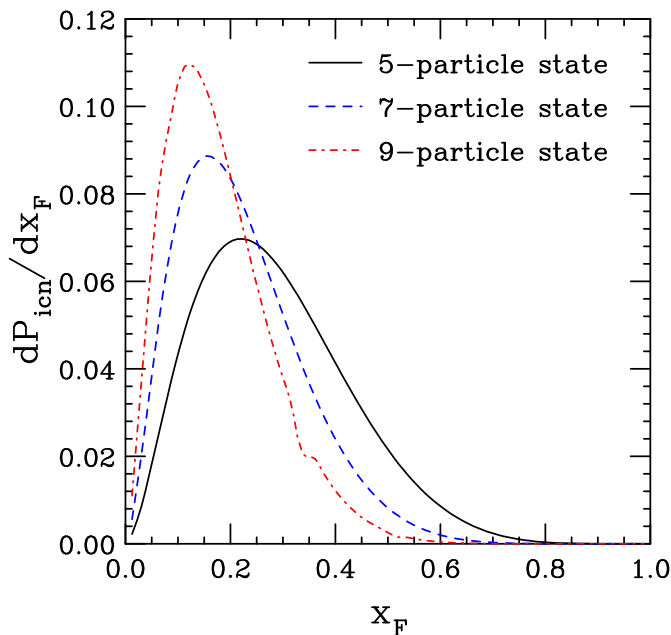


FIG. 8: The probability distribution as a function of x_F for charm quark production from 5- (solid black), 7- (dashed blue), and 9-particle states (dot-dashed red). All calculations use set kt2.

they are assumed to have the same current quark mass in the model.

The x_F distribution is shown in Fig. 8 because it is independent of energy and k_T range while the rapidity distribution is not. Because $x_F = (2m_T/\sqrt{s}) \sinh y$, for fixed m_T and y , the x_F value probed appears at higher rapidity with increasing \sqrt{s} . For example, if $x_F = 0.2$, near the average x of a charm quark in a 5-particle state, and $m_T = 2$ GeV, $y = \sinh^{-1}(0.05\sqrt{s})$ so that for $\sqrt{s} = 20$ GeV, in the range of prior fixed-target experiments measuring J/ψ and open charm; 100 GeV, near the top energy for $p + \text{Ar}$ measurements using the SMOG device at the LHC; and 5 TeV, in the lower range of LHC $p + p$ collisions; the y value corresponding to this x_F is 0.9, 2.3 and 6.2 respectively. The effective forward boost of calculating the intrinsic charm distribution as a function of rapidity over a wide range of \sqrt{s} is illustrated in Ref. [68]. Note also that the rapidity distributions, as shown later, can also depend on the k_T range of the integration because $x_F \propto m_T$.

The average x_F of the charm quark decreases as the number of quarks in the state. The average x_F of a charm quark in a 5-particle state of 0.285. If one adds only light $q\bar{q}$ pairs, the average x_F of a charm quark decreases to 0.220 for a 7-quark state and 0.178 for a 9-particle state. Note that, as a function of rapidity, the boosted distributions would retain the same hierarchy, with charm quarks from a 5-particle state at higher average rapidity than those from a 7- or 9-particle state.

The average transverse momentum of a charm quark,

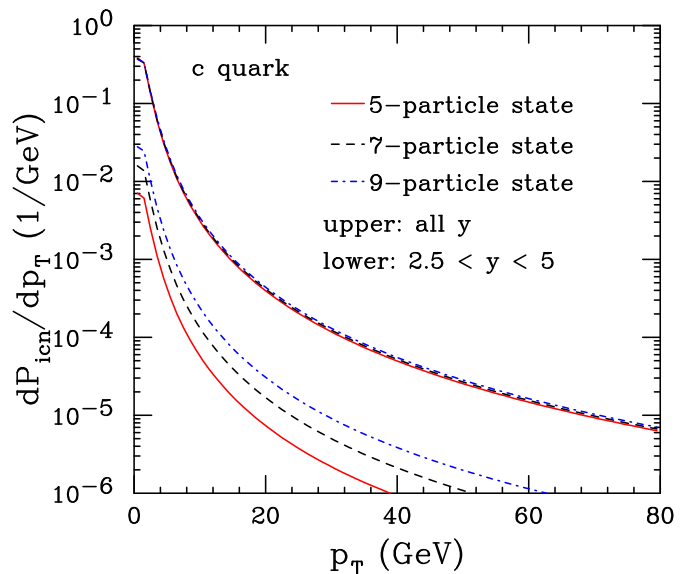


FIG. 9: The probability distribution as a function of p_T for charm quark production from 5- (solid black), 7- (dashed blue), and 9-particle states (dot-dashed red). All calculations use set kt2. The upper set of curves are integrated over all rapidity while the lower curves correspond to $2.5 < y < 5$ for $\sqrt{s} = 7$ TeV.

integrated over all x_F and rapidity, slightly increases with the number of quarks in the state. The increase is likely because the high p_T tail of the charm distribution is slightly harder for states with more particles: $\langle p_T \rangle = 2.32$ GeV for a 5-quark state; 2.37 GeV for a 7-quark state; and 2.40 GeV for a 9-quark state. The charm distribution becomes harder because the additional light quarks in the more populated states have a lower maximum k_T range. Note that if no kinematic constraints are included, such as the finite rapidity acceptance of a detector, the p_T distribution would be independent of energy [68]. Thus, at low fixed-target energies, the p_T distribution from intrinsic charm is broader than that from perturbative QCD but at higher energies, $\sqrt{s} > 40$ GeV, the two contributions become difficult to distinguish at higher p_T when no rapidity cuts are considered [68]. So far, poor experimental statistics at high p_T limit the potential determination of a large intrinsic charm contribution in this part of phase space, see the discussion in Ref. [66] for example.

As further shown in Ref. [68], the J/ψ and \bar{D} meson p_T distributions from intrinsic charm depend on the calculated rapidity range. This is demonstrated in Fig. 9 where the charm quark p_T distribution integrated over all x_F ($0 < x_F < 1$) is compared to that for an x_F range appropriate for $2.5 < y < 5$ at $\sqrt{s} = 7$ TeV, corresponding to $0.00454 < x_F < 0.0557$. As can be seen in Fig. 8, because the average x_F is reduced for states with more quarks, the p_T distribution from a 9-particle state encompasses more of the p_T distribution at this low x_F than

the 5- or 7-particle states. The energy dependence of the p_T distribution is discussed in more detail in Sec. VB.

The assumption of a fixed tetraquark mass in the calculation of the y and p_T distributions, in contrast to the mass distributions, means that the calculations are independent of whether the tetraquark is composed of a meson pair or four uncorrelated quarks. Thus the momentum-conserving delta functions and the additional delta functions needed to connect the four constituents of the tetraquark are all that are required in addition to Eq. (1). Thus the kinematic distributions are independent of any correlations between the partons in the state as long as the same number and type of partons are included. This observation was also made in Ref. [36].

With this starting point, the rapidity and p_T distributions are shown in Secs. VA and VB respectively.

A. Rapidity Distributions

State	\sqrt{s}		
	5 TeV	7 TeV	13 TeV
$T_{\psi\psi}(6600)$	5.96	6.30	6.91
$T_{\psi\psi}(6900)$	5.40	6.24	6.85
$X(3872)$	6.46	6.80	7.42
$X_s(\text{kt1})$	6.32	6.66	7.27
$X_s(\text{kt2})$	6.42	6.76	7.39
$X_s(\text{kt3})$	6.06	6.39	7.02
$X_s(\text{kt4})$	6.21	6.54	7.15
T_{cc}^-	6.27	6.61	7.23
$T_{c\bar{c}s}^-$	6.42	6.77	7.38
T_{cs}^0	6.56	6.40	7.51
T_{cs0}^a	6.34	6.68	7.30

TABLE VI: The average tetraquark candidate rapidity from intrinsic charm states for different LHC energies. Note that T_{cs}^0 refers to both T_{cs1}^0 and T_{cs0}^0 while T_{cs0}^a refers to both T_{cs0}^{a0} and T_{cs0}^{a+} .

The rapidity distributions are calculated for $\sqrt{s} = 5, 7$ and 13 TeV, all center of mass energies for $p+p$ collisions at the LHC. To facilitate comparison between tetraquark states, typically only results are shown for $\sqrt{s} = 7$ TeV. The average value of the rapidity is given for all energies in Table VI.

Figure 10 shows the rapidity distributions for the $T_{\psi\psi}(6600)$ and $T_{\psi\psi}(6900)$, obtained with the k_T ranges with sets kt2 and kt1 respectively. As expected, the distributions peak at rapidities greater than 5 with the furthest forward distributions being those at $\sqrt{s} = 13$ TeV. Because the $T_{\psi\psi}$ has the largest mass of all the tetraquark candidate states considered, it is boosted least.

The differences between the distributions based on mass (k_T range) are negligible on the scale of the plots.

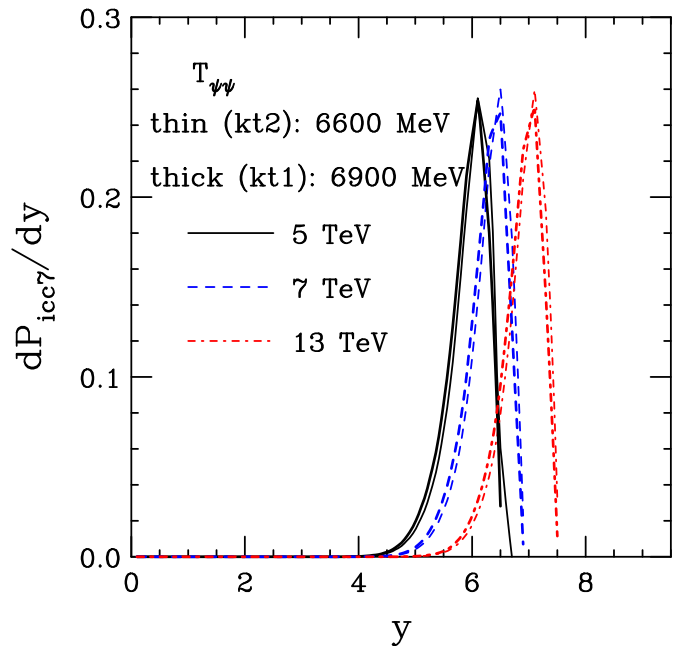


FIG. 10: The probability distribution as a function of rapidity for $T_{\psi\psi}$ production at $\sqrt{s} = 5$ (solid black), 7 (dashed blue), and 13 TeV (dot-dashed red). The thin lines, for $T_{\psi\psi}(6600)$, use set kt2 while the thick lines, for $T_{\psi\psi}(6900)$, use set kt1.

They are generally less than 0.1 unit of rapidity given the 300 MeV difference in mass.

All the distributions in this figure and, indeed, all the rapidity distributions shown in this section, have a characteristic shape due to the transformation from x_F to rapidity. There is a long tail from zero rapidity until just below the peak where the distribution abruptly climbs. The descent to the edge of phase space above the peak is very abrupt, nearly vertical. This seems almost counter-intuitive compared to the charm quark x_F distribution where the rise from $x_F = 0$ to the peak is faster than that descent above it as $x_F \rightarrow 1$. However, as noted in the discussion of Fig. 8, at $\sqrt{s} = 7$ TeV, while the boost affects all energies similarly, it is less pronounced at lower rapidity.

The $X(3872)$ rapidity distributions are shown for all three LHC energies in Fig. 11. They are calculated with set kt2, the set of k_T integration ranges that agree best with the measured $X(3872)$ mass. While the distributions are similar to those shown in Fig. 10, the lighter mass of the $X(3872)$ results in a more forward-peaked rapidity distribution.

Figure 12 shows the rapidity distributions for all four sets of k_T ranges for the X_s . Sets kt2, kt1 and kt4 correspond to the states measured at approximately 4.0, 4.5 and 4.9 GeV. The different masses and the associated k_T ranges affect the rapidity distributions. The most forward distribution is found for the lowest mass and narrowest k_T range, set kt2. The increased k_T range cor-

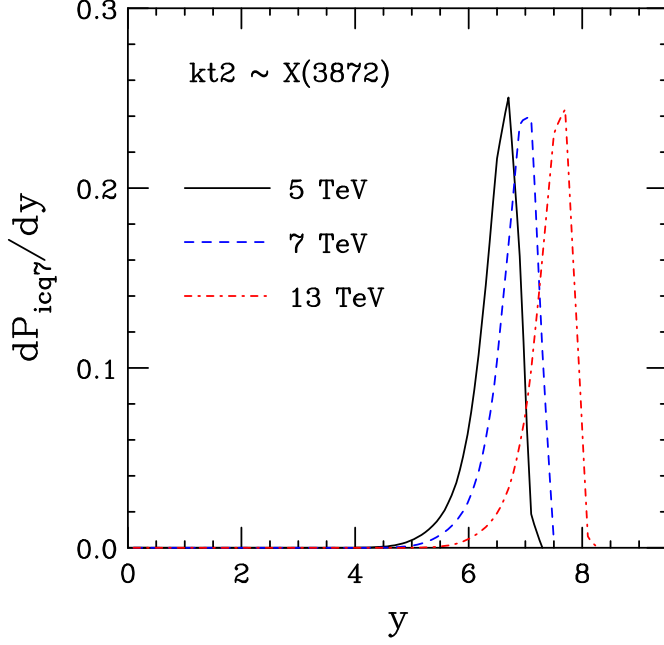


FIG. 11: The probability distribution as a function of rapidity for $X(3872)$ production at $\sqrt{s} = 5$ (solid black), 7 (dashed blue), and 13 TeV (dot-dashed red), all calculated using parameter set kt2.

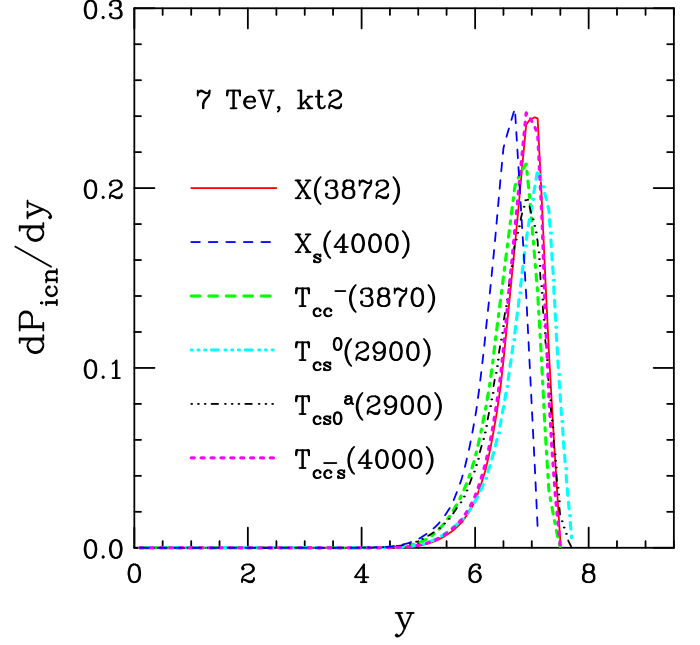


FIG. 13: The probability distribution as a function of rapidity at $\sqrt{s} = 7$ TeV using parameter set kt2 for $X(3872)$ (solid red), X_s (dashed blue), T_{cc}^- (dot-dashed green); T_{cs}^0 (dot-dot-dot-dashed black), T_{cs0}^a (dash-dash-dash-dotted cyan) and T_{ccs}^- (dotted magenta).

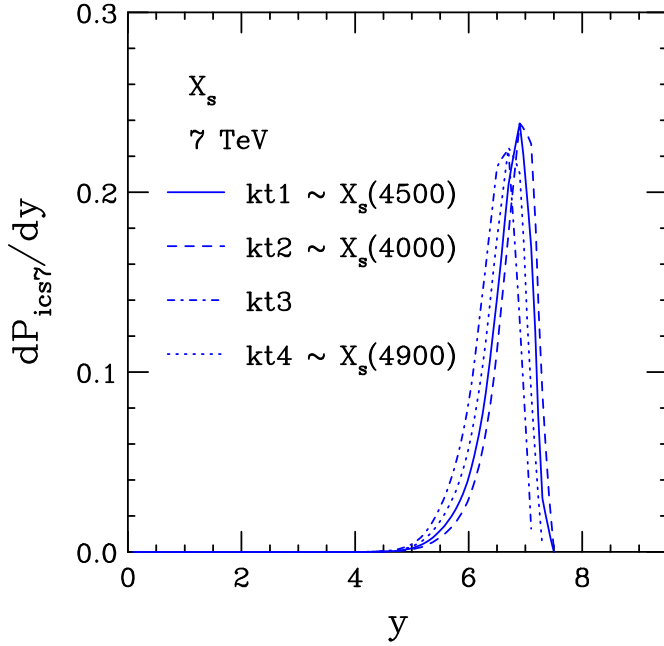


FIG. 12: The probability distribution as a function of rapidity for X_s production at $\sqrt{s} = 7$ TeV for parameter sets kt1 (solid), kt2 (dashed), kt3 (dot dashed) and kt4 (dotted). The approximately grouped X_s masses based on Table I are associated with the closest k_T range.

responding to higher masses shifts the distribution backward in rapidity so that set kt2 (mass 4.0 GeV) is forward of set kt1 (mass 4.5 GeV), with sets kt4 (mass 4.9 GeV) and kt3 (mass 5.4 GeV, see Table IV) peaking at lower rapidities. The rapidity shift due to the changes in mass and k_T range is on the order of 0.1 units of rapidity, similar to the difference noted for the $T_{\psi\psi}$.

Figure 13 compares all the rapidity distributions for tetraquark candidates with one or two charm quarks at $\sqrt{s} = 7$ TeV. All distributions are calculated for set kt2 so that the X_s distribution shown corresponds to the lowest mass state. The $X(3872)$, T_{cc}^- , and T_{ccs}^- all have similar quark content (at least two charm quarks) and masses, thus their rapidity distributions are also similar. Note that the exchange of a light quark for a strange quark in the T_{ccs}^- does not significantly affect the mass or rapidity. The X_s , with two strange quarks, has the lowest average rapidity.

The T_{cs}^0 , with a single charm quark, arising from a 7-particle state, is the most forward. It is worth noting that while the quark content is very similar to that of the T_{cs0}^a – one charm quark, one strange quark and two light quarks – the peak of the T_{cs0}^a is shifted backward by about 0.2 units of rapidity relative to the T_{cs}^0 . That is because the T_{cs0}^a must be produced from a 9-particle state. If a ‘non-leading’ 11-particle states had been considered, e.g. to produce the T_{cc}^+ instead of the T_{cc}^- , one could expect a similar small backward shift for rapidity distributions

from such states even though the quark content and mass are similar. This is clear from Fig. 8.

B. Transverse Momentum Distributions

The p_T distributions are now shown for the tetraquark candidates, under the same conditions as in Sec. V A.

		$\sqrt{s} = 5$ TeV		$\sqrt{s} = 7$ TeV		$\sqrt{s} = 13$ TeV	
	all y	$2.5 < y < 5$					
State	$\langle p_T \rangle$	% $P_{ic,n}$	$\langle p_T \rangle$	% $P_{ic,n}$	$\langle p_T \rangle$	% $P_{ic,n}$	$\langle p_T \rangle$
$T_{\psi\psi}(6600)$	4.05	3.40	21.74	1.52	30.32	0.33	47.50
$T_{\psi\psi}(6900)$	4.56	4.52	21.92	2.04	30.45	0.45	47.61
$X(3872)$	2.82	1.36	23.94	0.65	31.82	0.15	48.20
$X_s(\text{kt1})$	3.49	2.18	24.19	1.03	32.02	0.24	48.24
$X_s(\text{kt2})$	2.97	1.53	24.01	0.73	31.86	0.17	48.13
$X_s(\text{kt3})$	4.75	4.36	24.18	2.07	32.12	0.48	48.42
$X_s(\text{kt4})$	4.09	3.10	24.33	1.50	32.16	0.35	48.37
T_{cc}^-	3.93	2.76	24.18	1.34	31.96	0.31	48.15
T_{ccs}^-	2.98	1.92	24.81	0.93	32.11	0.21	48.29
T_{cs}^0	3.22	1.83	24.91	0.90	32.46	0.21	48.39
T_{cs0}^a	3.19	2.94	19.92	1.47	26.48	0.38	41.22

TABLE VII: The average tetraquark candidate p_T (in GeV) from intrinsic charm states for $p + p$ collisions at $\sqrt{s} = 5, 7$ and 13 TeV. At each energy, the percentage of the total p_T distribution captured in the rapidity range $2.5 < y < 5$ is given along with the average p_T at that energy. The average p_T integrated over all rapidity, independent of energy, is also shown. Note also that T_{cs}^0 refers to both T_{cs1}^0 and T_{cs0}^0 while T_{cs0}^a refers to both T_{cs0}^{a0} and T_{cs0}^{a++} .

The p_T distributions are again calculated for $\sqrt{s} = 5, 7$ and 13 TeV, all center of mass energies for $p + p$ collisions at the LHC. To facilitate comparison between tetraquark states, typically only results are shown for $\sqrt{s} = 7$ TeV. The average p_T value is given for all energies in Table VII. The averages are first given for the entire forward rapidity range and then assuming that the rapidity range covered is $2.5 < y < 5$. Because the amount of the total p_T distribution captured depends on the rapidity range, the percentage of the total probability for that energy and rapidity range is given as % $P_{ic,n}$.

While the average p_T calculated over all rapidities is rather moderate and similar to the average p_T of the charmonium states, albeit somewhat higher, when a finite rapidity region is considered, the average p_T increases by an order of magnitude and grows with center of mass energy while the percentage of the p_T distribution captured by the rapidity range decreases as the tetraquark candidate is boosted further forward in rapidity as \sqrt{s} increases.

The reason for this is illustrated in Figs. 14 and 15. As shown in Ref. [68], the relation between the Feynman x of the hadron created by coalescence of the constituent

quarks in the $J/\psi, \bar{D}$ meson, or charm tetraquark candidate, and rapidity means that, for a fixed value of x_F , the maximum p_T can be quite large according to the definition $x_F = (2m_T/\sqrt{s}) \sinh y$.

Because the tetraquark candidate in the intrinsic charm picture is comoving with the parent proton, it can manifest itself at rather high p_T , even at relatively high rapidity. For example, if $x_F = 1$ and $m_T = 1$ GeV, the maximum rapidity is $\sinh^{-1}(\sqrt{s}/2) = 8.85$ with $\sqrt{s} = 7$ TeV. If $m_T = \sqrt{s}/2$, then the maximum rapidity is $y = \sinh^{-1}(1) = 0.881$, near midrapidity, for the same energy. At $x_F \sim 0$, on the other hand, then $m_T \sim 0$ for any rapidity. Thus in Figs. 14 and 15, the p_T distribution, integrated over all rapidity, peaks at $p_T \sim 0$ and then decreases slowly with p_T until near the edge of phase space.

If, on the other hand, one considers a finite rapidity range, the distributions can behave quite differently, as shown in these figures at forward rapidity for $\sqrt{s} = 5, 7$ and 13 TeV. The maximum m_T in the forward rapidity range covered by LHCb, $2.5 < y < 5$, is 578.5 GeV for $y = 2.5$ and 47.2 GeV for $y = 5$, assuming $x_F \equiv 1$. Thus the low p_T part of the p_T spectrum is suppressed at forward rapidity. Increasing the center of mass energy from \sqrt{s} from 5 to 13 TeV consequently increases the suppression of the low p_T spectral contribution. However, as the p_T increases, the suppression is reduced until, at sufficiently high p_T (higher for larger \sqrt{s}), the spectrum is no longer suppressed and the distributions merge with that of the rapidity-integrated spectrum. This low p_T spectral suppression in a finite rapidity range leads to the large increase in the average p_T seen in Table VII. Assuming a lower rapidity range at the same center of mass energies would lead to greater suppression at low p_T and increase the average p_T still further. The maximum m_T is reduced for lower values of x_F .

Because $m_T = \sqrt{p_T^2 + m^2}$, for fixed m_T , a larger mass particle reduces the p_T range. The difference in the maximum p_T between the $T_{\psi\psi}$ mass of 6.6 or 6.9 GeV and that of the $X(3872)$ is small. However, one can observe a change in the spectral shapes for the $T_{\psi\psi}$ and the $X(3872)$ and, indeed, greater low p_T suppression for the more massive state.

In the remainder of this section, only distributions at $\sqrt{s} = 7$ TeV and in the rapidity range $2.5 < y < 5$ are shown to illustrate differences in the chosen k_T ranges (for X_s production) and the general makeup of the states themselves.

Figure 16 shows the p_T distributions at 7 TeV for the X_s states, including all four sets of k_T ranges, each calculated with the average mass given in Table IV. It is clear that the larger k_T range and corresponding larger mass results in a somewhat harder p_T distribution with a slightly higher peak. In the case of the lowest mass, kt2, the percentage of the p_T distribution captured in the rapidity range $2.5 < y < 5$, given as % $P_{ic,n}$, is the smallest with increasing fractions for sets kt1, kt4 and kt3 respectively, corresponding to broader k_T integration ranges.

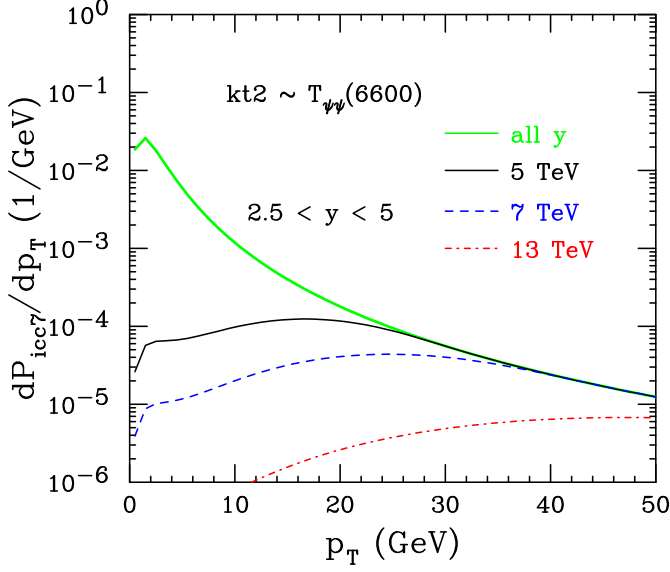


FIG. 14: The probability distribution as a function of p_T for $T_{\psi}(6600)$ production at $\sqrt{s} = 5$ (solid black), 7 (dashed blue), and 13 TeV (dot-dashed red), all calculated using parameter set kt2, corresponding to the mass of ~ 6600 MeV.

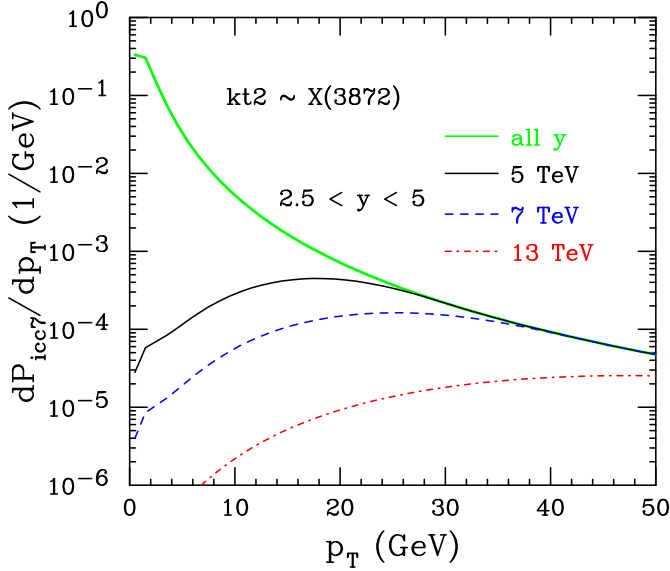


FIG. 15: The probability distribution as a function of p_T for $X(3872)$ production at $\sqrt{s} = 5$ (solid black), 7 (dashed blue), and 13 TeV (dot-dashed red), all calculated using parameter set kt2.

The average p_T integrated over all rapidity also increases with increasing k_T range and mass of the state, as observed in Table VII. The change in the average p_T is much smaller when the rapidity range is fixed to $2.5 < y < 5$.

Finally, the p_T distributions for tetraquark candidates with one and two charm quarks are compared in Fig. 17,

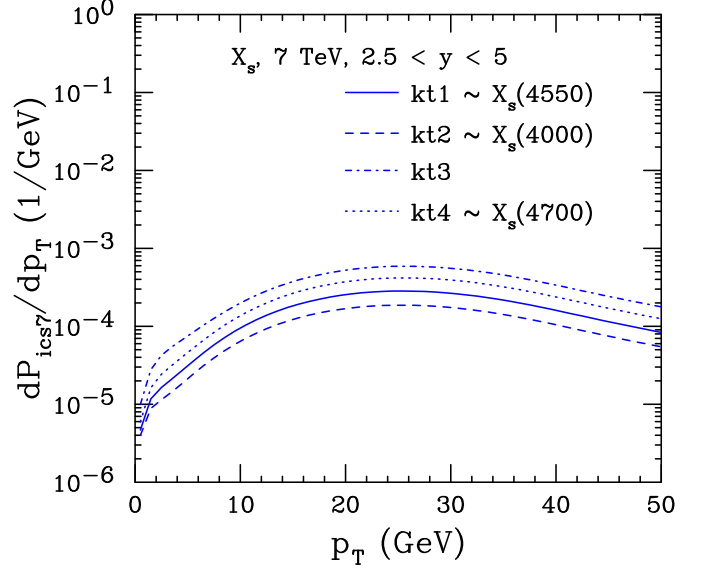


FIG. 16: The probability distribution as a function of rapidity for X_s production at $\sqrt{s} = 7$ TeV for parameter sets kt1 (solid), kt2 (dashed), kt3 (dot dashed) and kt4 (dotted). The approximately grouped X_s masses based on Table I are associated with the closest k_T range.

also at $\sqrt{s} = 7$ TeV. Here all the distributions are calculated with set kt2. Integrated over rapidity, the average p_T values for states with two charm quarks are all around 3 GeV. The average p_T of the T_{cs}^0 and T_{cs0}^a , with a single charm quark, are somewhat larger but the difference is small. When the rapidity cut is applied, the percentage of the distributions captured are all similar for the $X(3872)$, X_s , T_{cc}^- , $T_{c\bar{c}s}$ and T_{cs}^0 . However, the values of $\%P_{ic,n}$ are larger overall for the T_{cs0}^a because it is produced from a 9-particle state while the others are all produced from 7-particle states. The average p_T of the distribution within the rapidity range is also higher, see Table VII. The backward shift to lower p_T of the T_{cs0}^a distribution is also clear in Fig. 17.

VI. ESTIMATED CROSS SECTIONS

In this section, the estimated cross sections are briefly discussed. The production cross section for a single intrinsic $c\bar{c}$ pair from a 5-particle $|uudc\bar{c}\rangle$ configuration of the proton can be written as [73]

$$\sigma_{ic5}(pp) = P_{ic5}^0 \sigma_{pN}^{\text{in}} \frac{\mu^2}{4\hat{m}_c^2}. \quad (4)$$

The resolving factor of $\mu^2/4\hat{m}_c^2$ arises from a soft interaction, breaking the coherence of the Fock state [44]. This factor was introduced to calculate the cross section for intrinsic charm in Ref. [73]. Here $\mu^2 = 0.1 \text{ GeV}^2$ is assumed [70]. The inelastic cross section $\sigma_{pN}^{\text{in}} = 30 \text{ mb}$ is

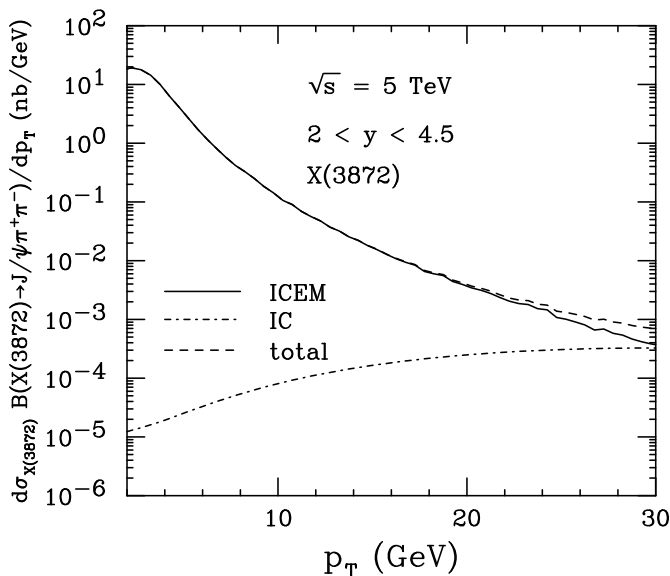


FIG. 19: The cross section of $X(3872)$ production as a function of p_T at $\sqrt{s} = 5$ TeV and $2 < y < 4.5$. The distribution calculated in the ICEM is shown by the solid line. The dot-dashed line gives the contribution from intrinsic charm in the rapidity range at this energy. The sum of the two is given by the dashed line.

compass the $X(3872)$ mass. Since the $X(3872)$ mass is only ~ 200 MeV larger than that of the $\psi(2S)$, the p_T distributions are effectively identical. The ICEM coefficient is adjusted to these data since no other data are available to determine the proper coefficient. The agreement of the calculation with the shape of the distribution is excellent. Applying this same coefficient, along with the upper bound of $P_{icc,7}^0$, gives the dot-dashed curve appearing in the bottom right corner. (Note that only the results from the LHCb Collaboration are shown here because the intrinsic charm contribution to $X(3872)$ production measured at more central rapidities by the CMS [75] and ATLAS [76] would not be visible on the plot.)

This result shows that at $\sqrt{s} = 13$ TeV, the contribution from intrinsic charm to the production of $X(3872)$ is negligible. This is not surprising given that average rapidity for the $X(3872)$ at this energy is 7.42, see Table VI. The boost is such that, in the rapidity range given in Table VII, $2.5 < y < 5$, only 0.15% of $P_{ic,n}$ is contained in that rapidity interval. Applying the interval measured by LHCb, $2 < y < 4.5$, would reduce that value still further. The average p_T in the given range is very high, $\langle p_T \rangle \sim 48$ GeV.

However, this does not rule out possible observation of tetraquark production by intrinsic charm at the LHC. The contribution could be more than a factor of 10 higher at $\sqrt{s} = 5$ TeV, with a peak at significantly lower p_T , see Table VII and Fig. 15. While the intrinsic charm contribution becomes larger at lower energies, due to the

decreased boost in rapidity, the perturbative production in an approach such as that of the ICEM, decreases so that the two may become more competitive, allowing the intrinsic charm contribution to become visible at high p_T , see Fig. 19.

VII. SUMMARY

The tetraquark mass and kinematic distributions have been studied in terms of the intrinsic charm model. The results suggest that a narrow k_T range, suggestive of tightly-bound partons is compatible with most of the measured tetraquark candidate masses. The mass distributions also suggest that, for tetraquark candidates with one or two charm quark constituents, the $X(3872)$, the X_s , and the T_{cc}^- are compatible with a meson pair structure for the tetraquark while, on the other hand, the T_{ccs}^- , the T_{cs}^0 and the $T_{cs_0}^a$ are more compatible with a loosely bound four-quark configuration.

The kinematic distributions calculated here, are assumed to be independent of the structure. At LHC energies, as studied here, the rapidity distributions are boosted to high rapidity while the p_T distributions are very hard, with a high p_T tail. These kinematics are considerably different than those obtained in perturbative QCD, as already noted for the J/ψ and \bar{D} mesons [68].

The potential cross sections in this approach are all small but could dominate production in regions of kinematic phase space where production by perturbative QCD mechanisms is small, namely at higher rapidity and transverse momentum, as shown in Ref. [66] for fixed-target J/ψ and \bar{D} production. However, the cross sections given in Sec. VI are total cross sections and do not include any reduction due to finite detector acceptance which could reduce them still further. As shown in Figs. 18 and 19, the intrinsic charm contribution to $X(3872)$ production is negligible at $\sqrt{s} = 13$ TeV but could become more visible at 5 TeV where the distribution is less boosted. If tetraquark candidates could be measured in either the fixed-target environment of the LHCb SMOG device or at the future electron-ion collider, one might see an even more significant effect due to intrinsic charm.

Finally, the same basic calculational structure can be applied to bottom tetraquarks, as was already done for a potential $X_b(b\bar{b}b\bar{b})$ state in Ref. [36]. This will be considered in future work.

Acknowledgments A. Angerami and V. Cheung are thanked for discussions. This work was supported by the Office of Nuclear Physics in the U.S. Department of Energy under Contract DE-AC52-07NA27344 and the LLNL-LDRD Program under Project No. 23-LW-036, and the HEFTY Collaboration.

- [1] S. K. Choi *et al.* [Belle Collaboration], Observation of a narrow charmonium-like state in exclusive $B^\pm \rightarrow K^\pm \pi^+ \pi^- J/\psi$ decays, *Phys. Rev. Lett.* **91**, 262001 (2003).
- [2] M. Ablikim *et al.* [BESIII Collaboration], Observation of a Charged Charmonium-like Structure in $e^+e^- \rightarrow \pi^+ \pi^- J/\psi$ at $\sqrt{s} = 4.26$ GeV, *Phys. Rev. Lett.* **110**, 252001 (2013).
- [3] Z. Q. Liu *et al.* [Belle Collaboration], Study of $e^+e^- \rightarrow \pi^+ \pi^- J/\psi$ and Observation of a Charged Charmonium-like State at Belle, *Phys. Rev. Lett.* **110**, 252002 (2013).
- [4] A. V. Evdokimov *et al.* [SELEX Collaboration], First observation of a narrow charm-strange meson $D_{sJ}^+(2632) \rightarrow D_s^+ \eta$ and $D^0 K^+$, *Phys. Rev. Lett.* **93**, 242001 (2004).
- [5] T. Aaltonen *et al.* [CDF Collaboration], Evidence for a Narrow Near-Threshold Structure in the $J/\psi \phi$ Mass Spectrum in $B^+ \rightarrow J/\psi \phi K^+$ Decays, *Phys. Rev. Lett.* **102**, 242002 (2009).
- [6] V. M. Abazov *et al.* [D0 Collaboration], Evidence for a $B_s^0 \pi^\pm$ state, *Phys. Rev. Lett.* **117**, 022003 (2016).
- [7] V. M. Abazov *et al.* [D0], Study of the $X^\pm(5568)$ state with semileptonic decays of the B_s^0 meson, *Phys. Rev. D* **97**, 092004 (2018).
- [8] <https://www.nikhef.nl/~pkoppenb/particles.html>
- [9] G. Aad *et al.* [ATLAS Collaboration], Observation of an Excess of Dicharmonium Events in the Four-Muon Final State with the ATLAS Detector, *Phys. Rev. Lett.* **131**, 151902 (2023).
- [10] A. Hayrapetyan *et al.* [CMS Collaboration], Observation of new structure in the $J/\psi J/\psi$ mass spectrum in proton-proton collisions at $\sqrt{s} = 13$ TeV, [arXiv:2306.07164 [hep-ex]].
- [11] R. Aaij *et al.* [LHCb Collaboration], Observation of structure in the J/ψ -pair mass spectrum, *Sci. Bull.* **65**, 1983-1993 (2020).
- [12] R. Aaij *et al.* [LHCb Collaboration], Observation of a Resonant Structure near the $D_s^+ D_s^-$ Threshold in the $B^+ \beta D_s^+ D_s^- K^+$ Decay, *Phys. Rev. Lett.* **131**, 071901 (2023).
- [13] R. Aaij *et al.* [LHCb Collaboration], Observation of $J/\psi \phi$ structures consistent with exotic states from amplitude analysis of $B^+ \rightarrow J/\psi \phi K^+$ decays, *Phys. Rev. Lett.* **118**, 022003 (2017).
- [14] R. Aaij *et al.* [LHCb Collaboration], Observation of New Resonances Decaying to $J/\psi K^{++}$ and $J/\psi \phi$, *Phys. Rev. Lett.* **127**, 082001 (2021).
- [15] R. Aaij *et al.* [LHCb Collaboration], Observation of an exotic narrow doubly charmed tetraquark, *Nature Phys.* **18**, 751-754 (2022).
- [16] R. Aaij *et al.* [LHCb Collaboration], Evidence of a $J/\psi K_S^0$ Structure in $B^0 \rightarrow J/\psi \phi K_S^0$ Decays, *Phys. Rev. Lett.* **131**, 131901 (2023).
- [17] R. Aaij *et al.* [LHCb Collaboration], First Observation of a Doubly Charged Tetraquark and Its Neutral Partner, *Phys. Rev. Lett.* **131**, 041902 (2023).
- [18] R. Aaij *et al.* [LHCb Collaboration], Amplitude analysis of the $B^+ \rightarrow D^+ D^- K^+$ decay, *Phys. Rev. D* **102**, 112003 (2020).
- [19] M. Gell-Mann, A schematic model of baryons and mesons, *Phys. Lett.* **8**, 214 (1964).
- [20] R. J. Jaffe, Multiquark hadrons. I. Phenomenology of $Q^2 \bar{Q}^2$ Mesons, *Phys. Rev. D* **15**, 267 (1977).
- [21] R. J. Jaffe, Multiquark hadrons: II. Methods, *Phys. Rev. D* **15**, 281 (1977).
- [22] S.-Q. Luo, K. Chen, X. Liu, Y.-R. Liu, and S.-L. Zhu, Exotic tetraquark states with the $qq\bar{Q}\bar{Q}$ configuration, *Eur. Phys. J. C* **77**, 709 (2017).
- [23] U. Kulshreshtha, D. S. Kulshreshtha and J. P. Vary, Hamiltonian, Path Integral and BRST Formulations of Large N Scalar QCD₂ on the Light-Front and Spontaneous Symmetry Breaking, *Eur. Phys. J. C* **75**, 174 (2015).
- [24] A. Esposito, A. Pilloni and A. D. Polosa, Multiquark Resonances, *Phys. Rept.* **668**, 1 (2017).
- [25] F.-K. Guo, C. Hanhart, U.-G. Meissner, Q. Wang, Q. Zhao, B.-S. Zou, Hadronic Molecules, *Rev. Mod. Phys.* **90**, 015004 (2018).
- [26] <https://qwg.ph.nat.tum.de/exoticshub/>
- [27] A. Cisek, W. Schäfer and A. Szczurek, Structure and production mechanism of the enigmatic $X(3872)$ in high-energy hadronic reactions, *Eur. Phys. J. C* **82**, 1062 (2022).
- [28] <https://www.exohad.org/>
- [29] R. L. Workman *et al.* [Particle Data Group], Review of Particle Physics, *Prog. Th. Exp. Phys.* **2022**, 083C01 (2022).
- [30] S. J. Brodsky, P. Hoyer, C. Peterson, and N. Sakai, The Intrinsic Charm of the Proton, *Phys. Lett. B* **93**, 451 (1980).
- [31] S. J. Brodsky, C. Peterson, and N. Sakai, Intrinsic Heavy Quark States, *Phys. Rev. D* **23**, 2745 (1981).
- [32] J. Badier *et al.* [NA3 Collaboration], Evidence for $\psi\psi$ Production in π^- Interactions at 150 GeV/c and 280 GeV/c, *Phys. Lett. B* **114**, 457 (1982).
- [33] J. Badier *et al.* [NA3 Collaboration], $\psi\psi$ Production and Limits on Beauty Meson Production From 400 GeV/c Protons, *Phys. Lett. B* **158**, 85 (1985).
- [34] R. Vogt and S. J. Brodsky, Intrinsic charm contribution to double quarkonium hadroproduction, *Phys. Lett. B* **349**, 569 (1995).
- [35] L. C. Bland *et al.* [ANDY Collaboration], Observation of Feynman scaling violations and evidence for a new resonance at RHIC, [arXiv:1909.03124 [nucl-ex]].
- [36] R. Vogt and A. Angerami, Bottom tetraquark production at RHIC?, *Phys. Rev. D* **104**, 094025 (2021).
- [37] M. Karliner, J. L. Rosner and S. Nussinov, $QQ\bar{Q}\bar{Q}$ states: masses, production and decays, *Phys. Rev. D* **95**, 034011 (2017).
- [38] Z.-G. Wang, Analysis of the $QQ\bar{Q}\bar{Q}$ tetraquark states with QCD sum rules, *Eur. Phys. J. C* **77**, 432 (2017).
- [39] Y. Bai, S. Lu and J. Osborne, Beauty-full Tetraquarks, *Phys. Lett. B* **798**, 134930 (2019).
- [40] J. Wu, Y.-R. Liu, K. Chen, X. Liu and S.-L. Zhu, Heavy-flavored tetraquark states with the $QQ\bar{Q}\bar{Q}$ configuration, *Phys. Rev. D* **97**, 094015 (2018).
- [41] G. Yang, J. Ping, L. He and Q. Wang, Potential model prediction of fully-heavy tetraquarks $QQ\bar{Q}\bar{Q}$ ($Q = c, b$), [arXiv:2006.13756 [hep-ph]].
- [42] X. Z. Weng, X. L. Chen, W. Z. Deng and S. L. Zhu, Systematics of fully heavy tetraquarks, *Phys. Rev. D* **103**, 034001 (2021).
- [43] R. J. Hudspith, B. Colquhoun, A. Francis, R. Lewis, and

- K. Maltman, Lattice investigation of exotic tetraquark channels, *Phys. Rev. D* **102**, 114506 (2020).
- [44] S. J. Brodsky, P. Hoyer, A. H. Mueller, and W.-K. Tang, New QCD production mechanisms for hard processes at large x , *Nucl. Phys. B* **369**, 519 (1992).
- [45] S. Paiva, M. Nielsen, F. S. Navarra, F. O. Duraes and L. L. Barz, Virtual meson cloud of the nucleon and intrinsic strangeness and charm, *Mod. Phys. Lett. A* **13**, 2715 91998).
- [46] M. Neubert, Heavy quark symmetry, *Phys. Rept.* **245**, 259 (1994).
- [47] F. M. Steffens, W. Melnitchouk, and A. W. Thomas, Charm in the nucleon, *Eur. Phys. J. C* **11**, 673 (1999).
- [48] T. J. Hobbs, J. T. Londergan and W. Melnitchouk, Phenomenology of nonperturbative charm in the nucleon, *Phys. Rev. D* **89**, 074008 (2014).
- [49] J. Pumplin, H. L. Lai, and W. K. Tung, The Charm Parton Content of the Nucleon, *Phys. Rev. D* **75**, 054029 (2007).
- [50] P. M. Nadolsky *et al.*, Implications of CTEQ global analysis for collider observables, *Phys. Rev. D* **78**, 013004 (2008).
- [51] S. Dulat *et al.*, Intrinsic Charm Parton Distribution Functions from CTEQ-TEA Global Analysis, *Phys. Rev. D* **89**, 073004 (2014).
- [52] P. Jimenez-Delgado, T. J. Hobbs, J. T. Londergan and W. Melnitchouk, New limits on intrinsic charm in the nucleon from global analysis of parton distributions, *Phys. Rev. Lett.* **114**, 082002 (2015).
- [53] R. D. Ball *et al.* [NNPDF Collaboration], A Determination of the Charm Content of the Proton, *Eur. Phys. J. C* **76**, 647 (2016).
- [54] R. D. Ball *et al.* [NNPDF Collaboration], Evidence for intrinsic charm quarks in the proton, *Nature* **608**, 483 (2022).
- [55] M. Guzzi, T. J. Hobbs, K. Xie, J. Huston, P. Nadolsky and C. P. Yuan, The persistent nonperturbative charm enigma, *Phys. Lett. B* **843**, 137975 (2023).
- [56] T. J. Hou *et al.*, CT14 Intrinsic Charm Parton Distribution Functions from CTEQ-TEA Global Analysis, *JHEP* **02**, 059 (2018).
- [57] J. Blumlein, A kinematic condition on intrinsic charm, *Phys. Lett. B* **753**, 619 (2016).
- [58] S. J. Brodsky, A. Kusina, F. Lyonnet, I. Schienbein, H. Spiesberger, and R. Vogt, A review of the intrinsic heavy quark content of the nucleon, *Adv. High Energy Phys.* **2015**, 341547 (2015).
- [59] S. J. Brodsky, G. I. Lykasov, A. V. Lipatov and J. Smiesko, Novel Heavy-Quark Physics Phenomena, *Prog. Part. Nucl. Phys.* **114**, 103802 (2020).
- [60] R. S. Sufian, T. Liu, A. Alexandru, S. J. Brodsky, G. F. de Téramond, H. G. Dosch, T. Draper, K. F. Liu and Y. B. Yang, Constraints on charm-anticharm asymmetry in the nucleon from lattice QCD, *Phys. Lett. B* **808**, 135633 (2020).
- [61] G. A. Alves *et al.* [E769 Collaboration], Enhanced leading production of D^\pm and $D^{*\pm}$ in 250 GeV π^\pm -nucleon interactions, *Phys. Rev. Lett.* **72**, 812 (1994).
- [62] E. M. Aitala *et al.* [E791 Collaboration], symmetries between the production of D^+ and D^- mesons from 500 GeV/c π^- -nucleon interactions as a function of x_F and p_T^2 , *Phys. Lett. B* **371**, 157 (1996).
- [63] M. Adamovich *et al.* [WA82 Collaboration], Study of D^+ and D^- Feynman's x distributions in π^- -nucleus interactions at the SPS, *Phys. Lett. B* **305**, 402 (1993).
- [64] LHCb Collaboration, Open charm production and asymmetry in p Ne collisions at $\sqrt{s_{NN}} = 68.5$ GeV, arXiv:2211.11633.
- [65] R. Vogt and S. J. Brodsky, Charmed hadron asymmetries in the intrinsic charm coalescence model, *Nucl. Phys. B* **478**, 311 (1996).
- [66] R. Vogt, Contribution from intrinsic charm production to fixed-target interactions with the SMOG Device at LHCb, *Phys. Rev. C* **108**, 015201 (2023).
- [67] T. Gutierrez and R. Vogt, Leading charm in hadron nucleus interactions in the intrinsic charm model, *Nucl. Phys. B* **539**, 189 (1999).
- [68] R. Vogt, Energy dependence of intrinsic charm production: Determining the best energy for observation, *Phys. Rev. C* **106**, 025201 (2022).
- [69] G. P. Lepage, A New Algorithm for Adaptive Multidimensional Integration, *J. Comput. Phys.* **27**, 192 (1978).
- [70] R. Vogt, Limits on Intrinsic Charm Production from the SeaQuest Experiment, *Phys. Rev. C* **103**, 035204 (2021).
- [71] V. Minissale, S. Plumari, Y. Sun, and V. Greco, Multi-charmed and singled charmed hadrons from coalescence: yields and ratios in different collision systems at LHC, *Eur. Phys. J. C* **84**, 228 (2024).
- [72] S. Cho, K.-J. Sun, C. M. Ko, S. H. Lee and Y. Oh, Charmed hadron production in an improved quark coalescence model, *Phys. Rev. C* **101**, 024909 (2020).
- [73] R. Vogt and S. J. Brodsky, QCD and intrinsic heavy quark predictions for leading charm and beauty hadroproduction, *Nucl. Phys. B* **438**, 261 (1995).
- [74] R. Aaij *et al.* [LHCb Collaboration], Measurement of $\chi_{c1}(3872)$ production in proton-proton collisions at $\sqrt{s} = 8$ and 13 TeV, *JHEP* **01**, 131 (2022).
- [75] S. Chatrchyan *et al.* [CMS Collaboration], Measurement of the $X(3872)$ Production Cross Section Via Decays to $J/\psi\pi^+\pi^-$ in pp collisions at $\sqrt{s} = 7$ TeV, *JHEP* **04**, 154 (2013).
- [76] M. Aaboud *et al.* [ATLAS Collaboration], Measurements of $\psi(2S)$ and $X(3872) \rightarrow J/\psi\pi^+\pi^-$ production in pp collisions at $\sqrt{s} = 8$ TeV with the ATLAS detector, *JHEP* **01**, 117 (2017).